Joint Centre for Mesoscale Meteorology, Reading, UK

Forecast skill of the ECMWF model using targeted observations during FAXTEX

A. J. Thorpe
A. Montani
R. Buizza
P. Unden

Internal Report No. 97

October 1998

Met Office Joint Centre for Mesoscale Meteorology Department of Meteorology
University of Reading PO Box 243 Reading RG6 6BB United Kingdom
Tel: +44 (0)118 931 8425 Fax: +44 (0)118 931 8791
www.metoffice.com

Designed and produced by the Met Office © Crown copyright 2001 01/0240 The Met Office logo is a registered trademark.

Forecast skill of the ECMWF model using targeted observations during FASTEX

A. Montani[1,*], A.J. Thorpe[1], R. Buizza[2], P. Unden[2]

[1]Department of Meteorology, University of Reading, UK

[2]European Centre for Medium–Range Weather Forecasts, Reading, UK

* Corresponding author: Andrea Montani, Department of Meteorology, University of Reading, Reading RG6 6BB, United Kingdom

Abstract

The impact of targeted observations on forecast accuracy is investigated for five case studies of cyclogenesis during the **F**ronts and **A**tlantic **S**torm **T**rack **EX**periment (**FASTEX**). Calculations of localised singular vectors (SVs) have been made from the ECMWF/IFS forecasting model to find the sensitive regions for each case study. Two sets of analyses have been prepared: a "control" set consisting of analyses in which all the FASTEX data have been removed from the operational analysis and a "perturbed" set obtained by adding to the control the data from the dropsondes deployed in regions highlighted as sensitive by SVs.

Analysis and forecast differences have been compared with the structure of the SVs as they evolve during the forecast.

Re–runs of the model, starting from the two different analyses, have been performed. The impact of the dropsonde data on the forecast skill has been assessed on the basis of both subjective (e.g. mean–sea–level pressure forecast errors) and objective (e.g. root–mean–square errors) scores. Experiments of sensitivity to the numbers of dropsondes used have also been performed. Re–runs of the model from perturbed analyses almost always give better objective scores than those starting from the control ones. The impact is more evident if the verification area coincides with the regions over which the SVs have been optimised. In this case, short–range prediction errors (up to day 2) are reduced on average by 15%, while, in the best case, the gain in predictability amounts to about 37%.

Changing the geographical location of a perturbation from a sensitive to a non–sensitive region has a dramatic impact on the growth of the disturbance. In both cases, the perturbation travels from the target to the verification region, but it does not grow when it is placed in a region that SVs indicate as non–sensitive.

Bishop and Toth (1996) suggest use of the Ensemble Transform Technique, where linear combinations of ensemble perturbations detect the variance of the prediction error associated with different configurations of the observational network. That particular configuration, which minimises the estimate of the forecast error variance, is considered the optimal one.

Another strategy is based on the use of potential vorticity maps to detect regions of incipient cyclone development (Hoskins et al., 1985; Davis and Emanuel, 1991), the target region being indicated by local potential vorticity maxima.

This paper concentrates only on the singular vector technique: the dominant singular vectors (hereafter, SVs) of the integral forward propagator of a non–linear dynamical system are used to predict Σ_i. The attention is focussed on the impact of the data from those dropsondes, deployed in regions highlighted as sensitive by SVs, on the forecast accuracy inside Σ_f.

SVs provide estimates of the time evolution of initial errors during the forecast (Lacarra and Talagrand, 1988; Farrell, 1990). SVs identify the fastest growing perturbations (according to a given norm) during a finite time interval and are operationally used at the European Centre for Medium–Range Weather Forecasts (ECMWF) to construct the initial perturbations of the Ensemble Prediction System (Buizza et al., 1993; Buizza and Palmer, 1995; Molteni et al., 1996).

A large cause of prediction error is related to that portion of analysis errors which project onto the growing phase space direction. The dominant SVs project along this direction. Following experiments (Buizza et al., 1997) which prove that forecast error can be reduced by perturbing the initial conditions with SV–generated perturbations, Montani et al. (1996) and Buizza and Montani (1998) show that only few SVs, calculated to maximise growth inside Σ_f, are needed to define Σ_i.

ECMWF SVs were used in real time, among other products, to target extra–observations during FASTEX and the impact of the observations on forecast accuracy is evaluated for five case studies of cyclogenesis during February 1997. The impact of the dropsondes was done using the ECMWF 3D–var data assimilation system as it was operational during FASTEX (IFS cycle 15R8) (see Courtier et al., 1998; Rabier et al., 1998; Andersson et al., 1998).

The methodology of targeting extra–observations using singular vectors is described in section 2. The assimilation and the time–evolution of the targeting signal is described in section 3. The results from the case studies analysed are reported in section 4 and

the last Δt hours of the time interval $(t_a,\ t_f)$, in order to provide the target region Σ_i at observing time t_i.

• The aircraft was sent to take extra–observations and the data obtained by the dropsondes were used to prepare new analyses from which to perform reruns of the forecast model.

During FASTEX, two different values for the forecast range (Δt) were used: 24 and 48 hours, while Δt_a was kept fixed at 36 hours. This implied $t_f - t_a = 60$ (and 84) hours. Since the size of the verification region was relatively small, only 10 SVs were calculated (5 for each configuration used).

To summarise, two sets of "FASTEX SVs" were daily computed at ECMWF: starting from the 0Z analysis of day *d*, a 84h (60h) forecast was run until the verification time, at 12Z of day *d+3* (*d+2*). The calculation of SVs was optimised over the last 48h (24h) of the trajectory. SVs so calculated were referred to as "+84/-48 SVs" ("+60/-24 SVs") and provided information for a flight occurring, in both configurations, at around 12Z of *d+1*. Since the targets indicated by ECMWF SVS were faxed from Reading to Shannon at around 5Z of day *d*, enough time (almost one and a half days) was left to alert the crew and prepare the flight plan.

This configuration had two main shortcomings: first, the fixed verification region proved to be slightly misplaced in those cases of cyclogenesis with the system tracking between Iceland and the British Isles. Secondly, FASTEX SVs provided target regions valid only at 12Z of a particular day, while there was a great variability in the take–off time of the research aircraft.

After FASTEX, SVs were re–calculated for a number of case studies of interest from a predictability point of view (see next section). In particular,

• the verification region was moved from case to case in order to include the minimum in the forecast mean–sea–level pressure of the cyclone;

• t_i was adjusted, relating it to the mid–flight time in the far–upstream area; t_f was moved to match it with the time of the system being around the British Isles;

• SVs were calculated with a shorter alert time ($\Delta t_a = 24$h) and also with zero alert time.

As investigated in Buizza and Montani (1998), the information provided by a particular set of SVs depends strongly on the accuracy of the forecast trajectory along which they are calculated. Typically, forecast skill is reduced as the prediction range increases. Therefore, the longer the forecast range, the higher is the risk of SVs indic-

of variables carry the information about the mass field and there is, to a large extent, a redundancy between them.

At the time of these recalculations, the 3D variational data assimilation system (3D–var) was operational at ECMWF. Then, analysis increments were calculated at T63 resolution (that is, about 210 km in grid–point space) and horizontal scales smaller than T63 could not be resolved. Higher resolution signals from closely–spaced dropsondes were damped and averaged at T63 by the data assimilation system. The advantage of a high resolution T213 model is to provide an accurate model background; then, the observation increments are calculated at high resolution and the remaining, necessary, analysis corrections at T63 are normally smaller than otherwise would be the case.

2.3 Definition of the target area using singular vectors

The initial structure of the most amplifying SVs can be used to identify the target region Σ_i where to take extra–observations. Consider the first M SVs at initial time written as $\nu_i(t_0)$ $(i = 1, \ldots, M$; usually, $M = 5)$ and let $T_i(s)$ be the temperature of the i–th SV at the grid point $s \equiv (\lambda, \phi, p)$, where λ denotes the longitude, ϕ the latitude and p the vertical coordinate. Analogous definitions can be used to identify $\xi_i(s)$, the relative vorticity of the i–th SV at a particular grid point.

Let $s_0 \equiv (\lambda_0, \phi_0, p_0)$ be the location where the first SV has its temperature maximum (either vorticity or potential vorticity could be chosen as well), that is

$$T_1(s_0) \geq T_1(s) \quad \forall s. \tag{1}$$

The target area can be identified by all the grid points s where the temperature perturbation, for any SV, is larger than a fraction of $T_1(s_0)$. After some experimentation, it was found that an appropriate fraction is about 0.6: this ensures that a significant number of grid points are included in Σ_i and, therefore, a reasonable geographical extension of the target region.

This means:

$$s \in \Sigma_i \text{ if and only if } T_i(s) \geq 0.6 \left(\frac{\sigma_1}{\sigma_i}\right) T_1(s_0), \quad \forall i = 1, \ldots M. \tag{2}$$

The weights σ_1/σ_i are introduced to take into account the fact that SVs with different ranking order grow with different amplification factors $(\sigma_1, \sigma_2, \ldots)$, the first one growing the fastest.

As shown previously (Buizza et al., 1993), temperature is good at providing information about SVs at initial time, since about 70% of SVs' total energy is in the potential

The above results show some dependence on the time of the dropsonde sounding. As the time difference between the dropsonde deployment and the analysis increases, the impact of the extra–information on the perturbed analysis is less evident, the smoothing on the dropsonde data being more marked.

Therefore, the data–assimilation system can incorporate local "non–standard" measurements in the perturbed analyses, providing a more accurate representation of the atmosphere. An interesting step forward would be to test the ability of more optimal data assimilation schemes (like 4–D var) to assimilate the extra–information provided by the FASTEX soundings.

3.2 Time evolution of the signal

Before analysing the relative accuracy of the control and perturbed reruns, it is important to discuss a few issues concerning SV targeting. A necessary condition for any targeting technique to be useful is that the signal, initially created in the analysis by the dropsonde data, travels from the target to the verification area. In the working hypothesis that the perturbed analysis is the best representation of the actual state of the atmosphere, the differences between the two analyses can be considered a reasonable estimate of the analysis error. Therefore, it is interesting to study the structure of these analysis differences and investigate how they evolve through the forecast. Also, the differences between the control and the perturbed forecasts provide information about the evolution of the targeting signal and can be compared to the evolving structure of the SV (calculated at intermediate times between t_i and t_f) and to the weather system under investigation. This enables one to understand interaction mechanisms between the basic state and perturbations fields. Therefore, analysis and forecast differences have been calculated at t_i and, then, every 6 hours until t_f. These fields have been compared to the 6–hourly linear evolutions of the SVs used to define the sensitive regions and to the analysis fields of the system investigated (available every 6 hours).

Here, typical results are presented for the cyclone developed between 18Z of 17 February and 12Z of 19 February (hereafter, t_i and t_f, respectively). This case study (IOP 17) has been chosen because the system is easily identifiable throughout its evolution and a link between basic state and SV fields can be easily established. Very similar results are found for the other FASTEX case studies we examined.

The first three rows in fig.2 show vertical cross sections of the fastest growing SV

(first row, plotted in terms of temperature), of the analysis and forecast differences between the control and the perturbed reruns (second row, plotted in terms of temperature) and of the basic state (third row, plotted in terms of relative vorticity). In each row, the panels represent the fields only at t_i, t_i + 24 hours, t_f (t_i + 42 hours). The direction of the cross sections change with time, but, at a fixed instant, it is the same for all quantities[1].

The last row shows vertical profiles of U, the basic state zonal wind (at t_i, t_i + 24 hours, t_f) at the point where the SV peaks.

At initial time, the zonal cross sections for the SV show a very marked westward tilt with height; the disturbance peaks in the middle and lower troposphere and is composed of elongated filaments of positive and negative anomalies. At the same time, the analysis differences (control minus perturbed analysis) show two regions of negative and positive anomalies evident in the lower and upper troposphere, respectively. Most of the structure is limited to the areas where the dropsondes were deployed, that is along the flight track of the research aircraft (shown in fig.3). The main peak in analysis difference (2.5°C at about 700 hPa) approximately coincides with the peak in SV structure, a secondary maximum being evident in the boundary layer at about 43N, 40W. The first panel of the third row shows that the basic state is characterised by a region of intense upper–level vorticity 12 degrees of longitude upstream of the SV. At low–levels, in the location of the analysis error and the SV maximum, a weak anticyclonic circulation is evident in a region located north of the surface cyclone (the region of positive relative vorticity corresponding to the centre of the storm is not captured by this cross section). The zonal wind, plotted where the SV (and the analysis differences) peaks, indicates easterlies in the lower troposphere and an intense westerly component in the middle and upper troposphere, peaking at tropopause level. Consequently, the upper portions of the targeting signal and of the SV will be advected eastwards faster than its lower portion, thus producing a change in the vertical structure of these fields.

The structure of the SV, plotted after 24 and 42 hours of linear evolution, indicates that the disturbance grows in amplitude (the contour interval at final time is four times the one used at t_i) and it becomes less tilted until it is nearly vertically stacked

[1]All the plotted fields are shown on 19 model levels. In the case of the SVs, they are all the levels available at the end of SV calculation; for the other fields, the 19 levels chosen are a subset of the 31 operationally available for basic state quantities. Then, although the y–labels of the first row are different from the others, the levels plotted in each panel are always the same.

4 Case study: IOP 17 (dropsondes from the G–IV flight)

In this section, IOP 17 (with the dropsonde data from the research aircraft G–IV) will be presented in detail, since this has been widely considered to be the best example of an Atlantic storm during FASTEX. Then, the other four case studies are dealt with in the next section. Basic information about the different case studies investigated are presented in table 1, which indicates, for each of the IOPs, the initial and final time of the control and perturbed reruns and the verification region.

IOP	t_i	t_f	Σ_f
9	18Z, 1 Feb	6Z, 3 Feb	52–67N, 5–25W
11	18Z, 4 Feb	6Z, 6 Feb	50–65N, 5–25W
12	18Z, 8 Feb	0Z, 10 Feb	55–68N, 12–32W
17 (G–IV)	18Z, 17 Feb	12Z, 19 Feb	50–65N, 0–20W
17 (Lear)	0Z, 18 Feb	12Z, 19 Feb	50–65N, 0–20W

Table 1: Information summary of the case studies investigated, providing the number of the IOP, the initial and final time of the forecast reruns and the verification region (t_i, t_f, Σ_f respectively).

The IOP 17 system was referred to in a Press Release as "The FASTEX Cyclone", with the lowest pressure (953 hPa) recorded during the experiment. It was also characterised by a very active cold front crossing the British Isles and causing some severe weather (72 knot gust in south–east England, 6 mm of rain in 6 minutes in Reading).

A brief description of the life–cycle of this system starts at around 12Z of the 17 February 1997. At that time, the low–level circulation in the North Atlantic is dominated by an intense westerly flow with a large–scale low located between Iceland and Greenland. A small low–pressure system, already with a developed structure, is evident south–west of Newfoundland (minimum of 1015 hPa at 37N 63W). The frontal zone is very elongated from west to east and both the front and the rear of the system seem alternative regions of incipient development. At upper levels, the flow is highly zonal with confluence just south of Newfoundland. Twelve hours later, the system has moved north–eastwards (1005 hPa at 40N 52W) with maxima in 700 hPa vertical velocity and low–level relative vorticity appearing just ahead of the low (not shown). From now on, the system travels more quickly north–eastwards, deepening especially once it enters the FASTEX Mesoscale Sampling Area (hereafter MSA), located around the British Isles. Between 12Z of 18 February and 12Z of the following day, the pressure

and the 3–D location (longitude, latitude and altitude) of the temperature maximum for each SV. Since the growth rates of the first two SVs are much higher than the others, information related only to SV=1 and 2 contributes, in practice, to the definition of Σ_i. In addition to this, the values found for the altitude of the targets are between 3 and 4 km: this confirms the importance of the the mid–lower troposphere as a favourable region for perturbation growth.

IOP	maximum at t_i	maximum at t_f
9	780	850
11	780	325
12	780	850
17 (G–IV)	700	850
17 (Lear)	700	850

Table 2: Approximate pressure level (in hPa) of the total energy maximum of the fastest growing SV at t_i and t_f, for all case studies investigated.

The importance of low–level structures is also evident in table 2, which gives for all the IOPs investigated, the pressure where the total energy of the fastest amplifying SV peaks at initial and final time.

At initial time, SV=1 has a marked energy peak at model level 13 (about 700 hPa), while at optimisation time, there is a broader structure, with maxima between about 325 hPa and 850 hPa, depending on the case. At t_i, the height of the energy peak is very typical for a SV (Molteni et al., 1996). However, surprisingly, the main peak is located in the lower troposphere (between 700 and 850 hPa) also at t_f. This seems to indicate a less efficient upward propagation of energy than that which often characterises SV evolution.

Reruns from both the control and the perturbed analyses were performed and the skill of the 42–hour forecast was tested against the verifying analysis, valid at 12Z of 19 February. In all the experiments, it was decided to use the best available verifying analyses, obtained by including in the operational ones most of the FASTEX extra–data (soundings, data from ships, dropsondes data, etc.). The improvement of the perturbed forecast has been assessed on the basis of both subjective (e.g., MSLP or low–level vorticity forecast errors, position errors) and objective scores (e.g., root–mean–square errors, hereafter rms[2]).

[2]The root–mean–square forecast error (over a specific region) is defined as $\frac{1}{N_i}\sqrt{\sum_i (f_i - a_i)^2}$, where f_i (a_i) is the value of a particular forecast (analysis) field at the grid point i, while N_i is the number of grid–points involved in the sum.

respectively. This improvement is higher than that over Europe, indicating the efficacy of the targeting technique in increasing the quality of a particular forecast range over a specified geographical region.

rms errors (m)	IOP 9 36h fc		IOP 11 36h fc		IOP 12 30h fc		IOP 17, G–IV 42h fc		IOP 17, Lear 36h fc	
	ctrl	drop	ctrl	drop	ctrl	drop	ctrl	drop	ctrl	drop
Z500	29	28	30	24	25	24	30	26	28	23
Z1000	40	40	45	38	39	43	59	40	68	43

Table 3: Case studies list and relative forecast range, Z500 and Z1000 root–mean–square forecast errors (in metres) inside the SVs' verification areas (as in table 1) for the control and the dropsonde–perturbed T213L31 reruns (denoted with "ctrl" and "drop", respectively).

Figs.6 also shows that the benefits gained by a better initialisation extend well beyond the 42–hour range, the perturbed forecast performing better up to and beyond day 3. The differences between the short–range forecasts is less evident as the verification region differs from the area for which the use of the dropsondes was designed. The impact is less dramatic if scores are considered over the North Atlantic, while there is no improvement at all in the amplitude of the prediction error over North Pacific (not shown). This is in full agreement with the philosophy of FASTEX, aiming to improve the forecasts locally and not necessarily globally by increasing the observational network only in specific sensitive areas.

Most of these previous remarks still hold for the rms errors of the 1000 hPa geopotential height. The gain in forecast accuracy over Europe and over the SVs' verification region is even more marked at 1000 rather than at 500 hPa, especially after forecast day 2, indicating a general benefit gained by the forecast at any level due to a more accurate initialisation (reduction of fast–growing analysis errors) in the sensitive areas.

5 Other case studies

Four additional case studies were investigated: IOP 17 with the Lear dropsondes, IOP 9, IOP 11 and IOP 12. In the next subsections, the impact of the dropsonde data on forecast accuracy is reported for each set of experiments. For reason of brevity, the synoptic descriptions are omitted, the attention being focussed on the impact of SV–directed targeted observations.

5.2 IOP 9

The low–pressure system investigated during IOP 9 is already mature in the far–upstream area. It moves away from the north–east coast of USA, crossing the Atlantic between 1 and 3 February.

The G–IV performed a flight in the developing region of the cyclone on 1 February. It took off from Shannon, Ireland, at 9Z and deployed two sets of dropsondes: the former one around Greenland, investigating a low pressure system which was going to verify outside the MSA; the latter one to the north–east of Newfoundland in order to sample the sensitivity regions of the cyclone in question. It landed in Goose Bay, Canada, at 15.30Z, after deploying, in total, 30 dropsondes. Here, the interest is focussed on the second set of dropsondes.

Because of the length of the flight, not all the dropsondes could be assimilated in the 12Z analysis cycle, which can only make use of the data available between 9Z and 15Z. A few dropsondes were deployed after 15Z and were incorporated in the following analysis cycle. In order to maximise the impact of the dropsonde data on the preparation of the perturbed reruns, analyses were cycled in the the following way:

- a perturbed 12Z analysis was prepared using the data from the dropsondes deployed between 9Z and 15Z, plus the information provided by the operational *first–guess* forecast run 6 hours before and by the standard observational network (without any other FASTEX data);
- a 6–hour forecast was run from the 12Z perturbed analysis;
- the 18Z perturbed analysis was obtained combining such short–range forecast with the data provided by those dropsondes deployed after 15Z (plus standard no–FASTEX observational network);
- the actual reruns (control and perturbed ones) started at 18Z.

The problem of selecting the dropsondes deployed in the sensitive regions at 12Z and 18Z was tackled by calculating two sets of SVs, one for each of these times. The verification time was kept fixed at 6Z of 3 February, as well as the verification region, extending from 52N to 67N and from 5W to 25W. Then, the two sets of SVs had two different Δt: 42 and 36 hours, respectively.

Fig.9 shows the locations of the maxima of the fastest growing perturbations plotted in terms of temperature as in equation (2). SVs do not indicate a sensitive region of limited geographical extension, within the flight range of a research aircraft. The area highlighted as sensitive is much larger than in the previous case studies, extending (at

higher than the control one. Similar remarks hold for the rms errors at 1000 hPa, with a greater forecast error reduction over Europe for the perturbed rerun from day 1.5 onwards.

In this case study, the impact of the dropsonde data was neutral at verification time, the 36–hour perturbed and the control reruns performing approximately the same. The positive consequences of the extra–information provided at initial time become more and more evident as the forecast range is increased and verification regions located farther downstream are considered.

5.3 IOP 11

This case consists of a primary cyclone which formed over the east coast of North America and deepened while crossing the Atlantic. Three upstream flight were performed in order to investigate the initiation region of the cyclone. Here, the attention is focussed on the flight of the US C–130, which took off at 11.20Z of 4 February and landed at 21Z of the same day in St. John's, Newfoundland, after deploying 19 dropsondes to the south and to the south–east of Newfoundland. As in the previous case study, the duration of the flight made it necessary to calculate two sets of SVs: the former one valid at 12Z (Δt = 42 h), the latter one at 18Z of 4 February (Δt = 36 h). The verification time was kept fixed at 6Z of 6 February as well as the verification region, extending from 50N to 65N and from 5W to 25W.

At both 12Z and 18Z, the most sensitive regions are located at around 700 hPa (see fig.11), corresponding to a meridional temperature gradient at that level and just downstream of a mid–tropospheric trough with a peak in low–level relative vorticity. As in the previous case studies, the target region is located on the right entrance of the 250 hPa jet maximum. The vertical distribution of total energy of the fastest growing SV (as in table 2) is very similar to that presented in Buizza and Palmer (1995), with a low–tropospheric maximum at initial time, and an optimisation time peak located at the tropopause level.

Only SV=1 and 2 contribute to the definition of Σ_i, since the amplification factors of the lesser growing perturbations are too small to satisfy the requirements of equation (2). A comparison between the flight track and the top picture of fig.11 seems to indicate a mismatch between the target region and the leg of the US C–130 flight at 41N, from 56W to 40W. In particular, the flight track seems located too much to the south in comparison with Σ_i. Nevertheless, the lower–tropospheric structure of

with an error of about 9 hPa, while the 1-drop rerun reduces this error, although by only 1 hPa. Nevertheless, both the control and the 1-drop forecasts are quite poor in locating the position of low minimum (just to the north-west of Scotland), misplacing it to the south. The inclusion of all the dropsonde data is necessary in order to improve the predictability of both the cyclone depth and its location (error reduced to 6hPa).

5.4 IOP 12

This is probably the most interesting FASTEX case study from a predictability point of view, since it was characterised by a massive divergence in forecasts between the various NWP models used during the experiment. In addition to this, the impact of targeted observations on forecast accuracy proved to be quite controversial and, for this reason, has been analysed in detail.

The system is a typical example of explosive cyclogenesis, occurring between 8 and 10 February and deepening rapidly as it enters the north-west part of the MSA. The G-IV took-off on 8 February at 10Z from Shannon, landing at 15.30Z in St. John's, performing a double-mission flight. In addition to deploying 10 dropsondes between 10W and 30W (at 53N) in order to study a system already mature in the MSA, the aircraft used 18 dropsondes west of 42W (between 48N and 52N) to investigate the sensitive regions for IOP 12. The data from the second set of dropsondes proved to have a big impact on the predictability of this cyclone.

In order to select the dropsondes to be used for the perturbed rerun, SVs were calculated between 12Z of 8 February and 0Z of 10 February, the verification region extending from 55N to 68N and from 12W to 32W. Since the last dropsondes were deployed after 15Z, SVs were calculated to find the sensitive regions also at 18Z of the same day (with the same verification time and region as before). Nevertheless, more weight was given to the information provided by the 12Z perturbations, since most of the dropsondes were assimilated in the 12Z cycle.

Fig.13 shows the target area according to the fastest growing perturbations at 12Z. Only the first two SVs determine the target region, since their growth rates are so large. All the SVs peak in the lower troposphere, just below 700 hPa, to the east and to the south-east of Newfoundland. Energy is maximum in the lower troposphere at both initial and final time (see table 2), with a less marked upward propagation of total energy.

The target region is located in an area characterised by a tight horizontal tem-

6 Summary of the results

In order to have an overall idea of the impact of targeted observations on forecast accuracy, the prediction uncertainties of the control and dropsonde reruns have been summarised in the scatter plots of fig.15. In the upper plot (from Undén et al., 1998), the 48, 60 and 72–hour rms forecast errors of the two sets of reruns have been reported in terms of Z500 and Z1000 (in metres), verifying over Europe and the North Atlantic.

Since five case studies, three prediction ranges, two verification regions and two variables are considered, there are, in total, 60 points in the diagram, each of them corresponding to a pair of control–perturbed forecast errors. The x–axis ("With Dropsondes" in the figure) reports the rms errors of the perturbed reruns, the y–axis ("Without Dropsondes") representing the performance of the control ones.

If most of the points are below the dashed line, targeted observations, according to localised SVs, would not be of great help for forecast improvement. But the figure shows that the majority of the points lies in the upper half of the plot, where the rms errors of the dropsonde reruns are lower than those of the control ones.

The lower plot is valid for the 30, 36, 42 and 48–hour rms forecast errors, verifying over the SVs' verification regions (changing from case to case according to table 1). The positive impact of the dropsonde data is even more evident than before. Very few points are located below the dashed line at 45° and the error reduction is particularly evident for those cases of large prediction errors for the control rerun (y–axis). On average, the gain in forecast accuracy amounts to about 15%, the highest error reduction being about 37%.

7 Sensitivity to the location of a perturbation

In order to show that sensitive regions do indeed exist and that the evolution of a perturbation changes dramatically if it is, or is not, located in a sensitive area, two experiments, described in fig.16, have been carried out. We aim to show that, by locating a perturbation in a predicted "non–sensitive" region and creating a new forecast, this perturbation can propagate into the verification region, but, as predicted, it does not grow in amplitude.

A perturbation (hereafter, sensitive perturbation; top right panel of the figure) has been initially located in the sensitive region, indicated by the SVs calculated for IOP 17 (G–IV flight). Then, it has been displaced from its initial geographical location. The

SV maxima and large basic state relative vorticity has not been found.

Although the SV energy initially peaks in the lower troposphere, there is a non–negligible downward propagation of energy with time (in addition to upwards), the maximum at optimisation time often being located just above the boundary layer (see table 2). The assimilation and the evolution of the targeting signal has been studied, showing that the data assimilation system operates a smoothing on the dropsonde information (for example, in terms of temperature and wind speed) when this is incorporated in the perturbed analysis.

Initial differences between the control and the perturbed analyses are vertically stacked at t_i and, then, propagate from the target to the verification region, growing in amplitude during the evolution. Forecast differences exhibit an increasing eastward tilt with height, as the range increases. This is due to differential advection of the targeting signal at lower and upper levels. Therefore, the portion of the targeting signal travelling in the upper troposphere, gets to the verification region before the targeted system itself. On the other hand, SVs initially tilt westwards with height and they are stacked vertically at optimisation time, over the verification region. Hence, in the middle and upper–troposphere, the targeting signal is ahead of the evolving SV at intermediate times between t_i and t_f. Only below 700 hPa, the two pieces of information travel together, as if both signals were "pivoting" around the levels just above the boundary layer. During the evolution and also at optimisation time, the system (plotted in terms of basic state relative vorticity) is slightly downstream of the SV and the forecast difference maximum.

Control and perturbed reruns have been performed and the accuracy of the two forecasts assessed on the basis of subjective and objective scores. In the five case studies examined, the perturbed reruns have lower rms forecast errors (in terms of geopotential height) than the control ones, the only exception being the surface errors for IOP 12, when the dropsonde data have a negative impact on forecast accuracy. Inside the SVs' verification regions, the errors in the perturbed reruns are reduced on average by 15%, the gain in prediction accuracy being more evident (up to 37%) for those cases of larger control forecast errors. In some case studies, the forecast improvement can also be seen on synoptic weather charts, the perturbed reruns being closer to the verifying analysis in predicting the location and the intensity of the surface low. If the verification region is increased to include either Europe or the North Atlantic, then the positive impact of the extra–data in sensitive regions is still evident, although less marked.

References

Andersson, E., Haseler, J., Unden, P., Courtier, P., Kelly, G., Vasiljević, D., Branković, C., Cardinali, C., Gaffard, C., Hollingsworh, A., Jakob, C., Janseen, P., Klinker, E., Lanzinger, A., Miller, M., Rabier, F., Simmons, A., Strauss, B., Thepaut, J–N., Viterbo, P., 1998. The ECMWF implementation of three–dimensional vatational assimilation (3D–var). III: Experimental results. *Quart. J. Roy. Meteor. Soc.*, **124**, 1831–1860.

Bishop, C.H. and Toth, Z., 1996. Using ensemble to identify observations likely to improve forecasts. American Meteorological Society pre-prints of the 7th conference on mesoscale processes, 9–13 September 1996, Reading, UK, pp. 618.

Buizza, R., Tribbia, J., Molteni, F., Palmer, T.N., 1993. Computation of optimal unstable structures for a numerical weather prediction model. *Tellus*, 45A, 388–407.

Buizza, R., Palmer, T.N., 1995. The singular–vector structure of the atmospheric global circulation. *J. Atmos. Sci.*, **52**, 1434–1456.

Buizza, R., Gelaro, R., Molteni, F., Palmer, T.N., 1997. The impact of increased resolution on predictability studies with singular vectors. *Quart. J. Roy. Meteor. Soc.*, **123**, 1007–1033.

Buizza, R. and Montani, A., 1998. Targeting observations using singular vectors. Submitted to *J. Atmos. Sci.*, .

Clough, S. A., Lean, H.W., Roberts, N.M., Birkett, H., Charboureau, J–P., Dixon, R., Griffiths, M., Hewson, T.D., Montani, A., 1998. A JCMM overview of FASTEX IOPs. Internal Report 81. Available from: Joint Centre for Mesoscale Meteorology, Dept. of Meteorology, Earley Gate, Reading, UK.

Courtier, P., Andersson, E., Heckley, W., Pailleux, J., Vasiljević, D., Hamrud, M., Hollingsworh, A., Rabier, F., Fisher, M., 1998. The ECMWF implementation of three–dimensional vatational assimilation (3D–var). I: Formulation. *Quart. J. Roy. Meteor. Soc.*, **124**, 1783–1807.

Davies, C.A. and Emanuel, K.A., 1991. Potential vorticity diagnostics of cyclogenesis.

Mon. Weather Rev., **119**, 1929–1953.

Farrell, B.F., 1990. Small error dynamics and the predictability of atmospheric flows. *J. Atmos. Sci.*, **47**, 2409–2416.

Gelaro, R., Buizza, R., Palmer, T.N., Klinkler, E., 1997. Sensitivity analysis of forecast errors and the construction of optimal perturbations using singular vectors. To appear in *J. Atmos. Sci.*, .

Hoskins, B.J., Mc Intyre, M.E., Robertson, A.W., 1985. On the use and significance of isentropic potential vorticity maps. *Quart. J. Roy. Meteor. Soc.*, **111**, 877–946.

Joly, A., Thorpe, A.J., Lemaitre, Y., Browning, K.A., Lalaurette, F., 1994. FASTEX: Fronts and Atlantic Storm–Track Experiment. Scientific papers. available from the FASTEX Project Office, February 1994, pp. 60.

Joly, A., Jorgensen, D., Shapiro, M.A., Thorpe, A.J., Bessemoulin P., Browning, K.A., Cammas, J–P., Chalon, J–P., Clough, S.A., Emanuel K.A., Eymard, R., Gall, R., Hildebrand, P.H., Langland, R.H., Lamaitre, Y., Lynch, P., Moore, J.A., Persoon, P.O.G., Snyder, C., Wakimoto, R.M., 1996. The Fronts and Atlantic Storm–Track Experiment (FASTEX): Scientific objectives and experimental design. Report Number 6. The FASTEX Project Office, Meteo–France, CNRM, 42 Avenue Coriolis, Toulouse, France.

Joly, A. et al., 1998. The Fronts and Atlantic Storm–Track Experiment (FASTEX) overview. To appear in *Quart. J. Roy. Meteor. Soc.*, .

Lacarra, J–F., Talagrand, O., 1988. Short range evolution of small perturbations in a barotropic model. *Tellus*, **40a**, 81–95.

Langland, R.H., Elsberry, R.L., Errico, R.M., (1995). Evaluation of physical processes in an idealised extra-tropical cyclone using adjoint sensitivity. *Quart. J. Roy. Meteor. Soc.*, **121**, 1349–1386.

Molteni, F., Buizza, R., Palmer, T.N., Petroliagis, T., 1996. The ECMWF Ensemble Prediction System: Methodology and validation. *Quart. J. Roy. Meteor. Soc.*, **122**, 73–119.

Figure captions

Figure 1: Vertical profiles valid at 18Z of 17 February 1997: difference between the control analysis and the dropsonde data (dotted line) and between the perturbed analysis and the dropsonde data (solid line). The top panel plots temperature profiles (in Kelvin) and the bottom one U, the zonal wind speed (in m/s), both at 43.6N 42.1W. In all the plots, the y–axis reports pressure (in hPa).

Figure 2: Vertical cross sections of the first SV (plotted in terms of temperature, first row), of the differences between the control and the perturbed rerun (plotted in terms of temperature, second row), of the basic state relative vorticity (third row) and vertical profile of the basic state zonal wind (fourth row). The fields are plotted at initial time (t_i: 18Z of 17 February 1997, first column), after 24 hours (second column) and after 42 hours (t_f: 12Z of 19 February 1997, third column). The direction of the cross sections are: from 43N, 70W to 43N, 30W (t_i); from 35N, 45W to 60N, 15W (t_i + 24h), from 50N, 20W to 70N, 10E (t_f). The vertical profile of the zonal wind is reported at 43N, 55W (t_i), at 48N, 29W (t_i + 24h), at 55N, 12W (t_f). Contour intervals for the SV: 0.025°C (t_i), 0.05°C (t_i + 24h), 0.1°C (t_f). Contour interval for the temperature differences: 1°C. Contour interval for the basic state relative vorticity: $6 \cdot 10^{-5}$ s^{-1}. Interval for the zonal wind: 10 m/s. The y–axes in all panels are model levels.

Figure 3: Observation summary for IOP 17 (from Clough et al., 1998).

Figure 4: IOP 17 (G–IV flight). Top picture: sensitive regions plotted in temperature, as in equation (2), according to the first 4 SVs, valid at 18Z of 17 February. Bottom picture: temperature structure of SV=1, valid at the same time, at around 700 hPa (contour interval: 0.03°C).

Figure 5: IOP 17 (G–IV flight): distributions in mean–sea–level pressure (left panels) and 850 hPa relative vorticity (right panels) valid at 12Z of 19 February: verifying analysis (top row), 42–hour control forecast (middle row) and 42–hour perturbed forecast (bottom row), both verifying at the same time. Contour interval: 4 hPa (left panels) and $8 \cdot 10^{-5} s^{-1}$ (right panels).

Figure 6: IOP 17 (G–IV flight): rms errors of the 500 hPa geopotential height (in metres) for three different verification areas: Europe (top left panel), North Atlantic (top right panel) and SVs' verification region (as in table 1, bottom panel), comparing the control forecast (marked "cntl", dashed lines) with the perturbed one (marked "drop", solid lines). All forecasts start at 18Z of 17 February 1997.

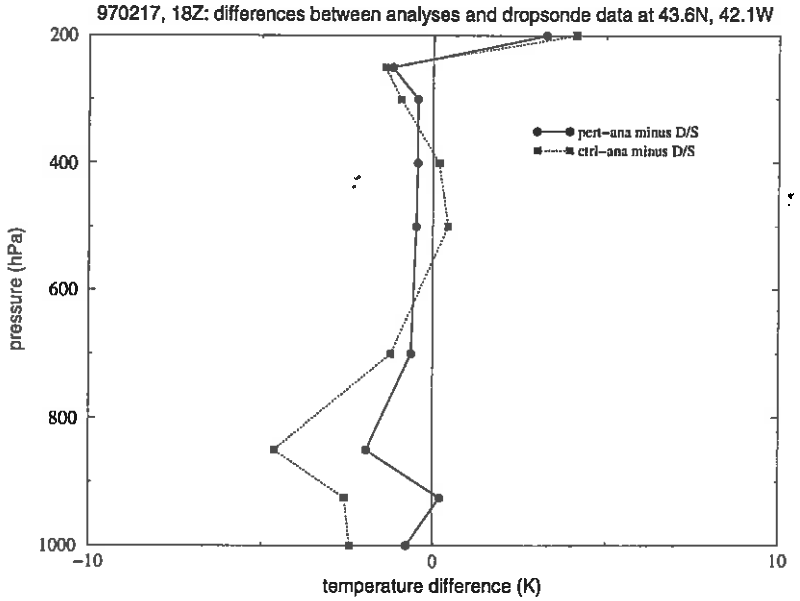
970217, 18Z: differences between analyses and dropsonde data at 43.6N, 42.1W
pert−ana minus D/S
ctrl−ana minus D/S
pressure (hPa)
200
400
600
800
1000
−10
0
10
temperature difference (K)

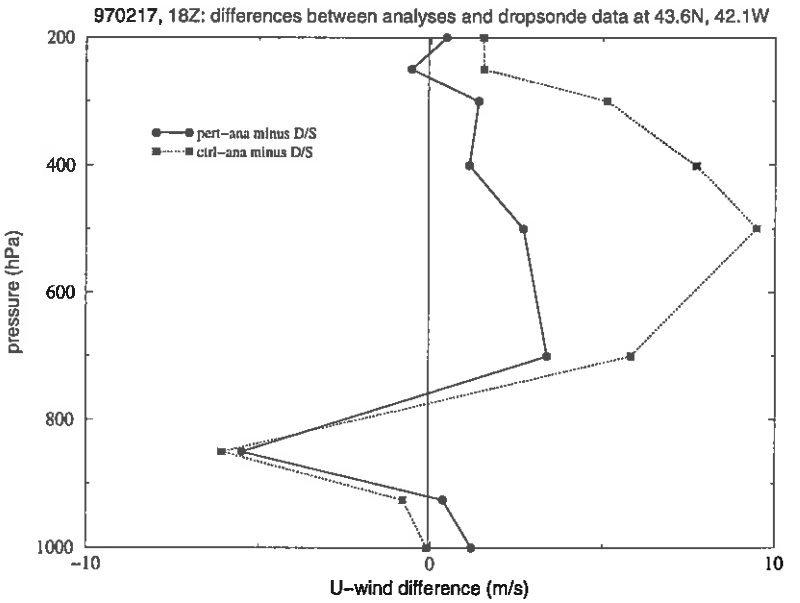
970217, 18Z: differences between analyses and dropsonde data at 43.6N, 42.1W
pert−ana minus D/S
ctrl−ana minus D/S
pressure (hPa)
200
400
600
800
1000
−10
0
10
U−wind difference (m/s)

FIG. 1

FASTEX IOP17 Low 41 15Z 17/02/97 - 15Z 19/02/97

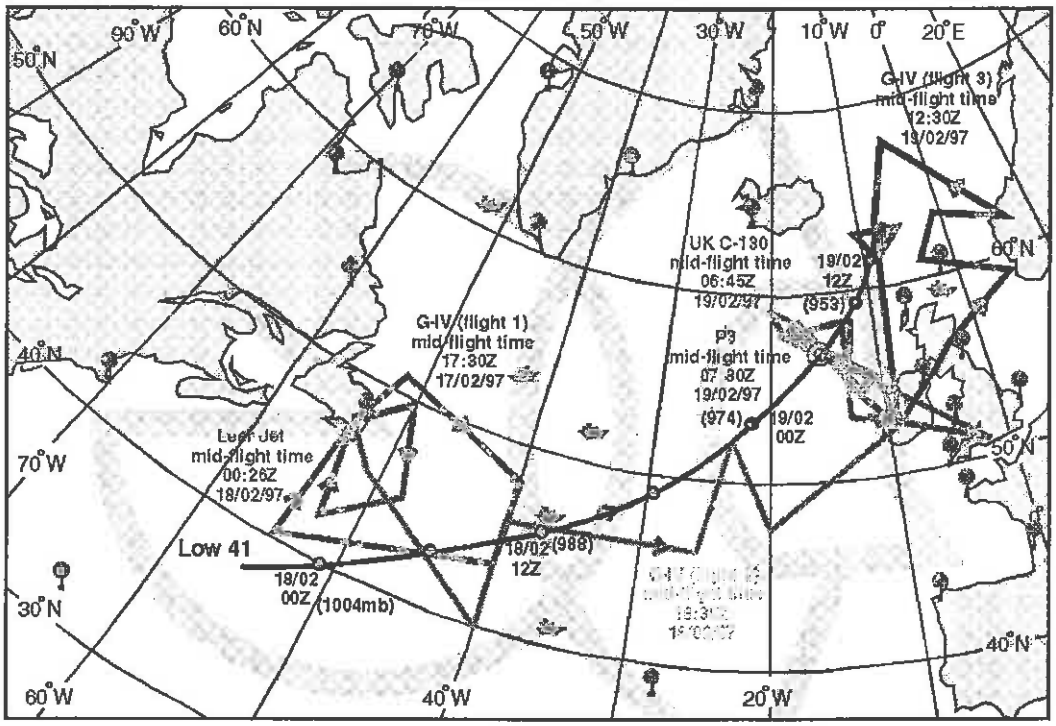

FIG. 3

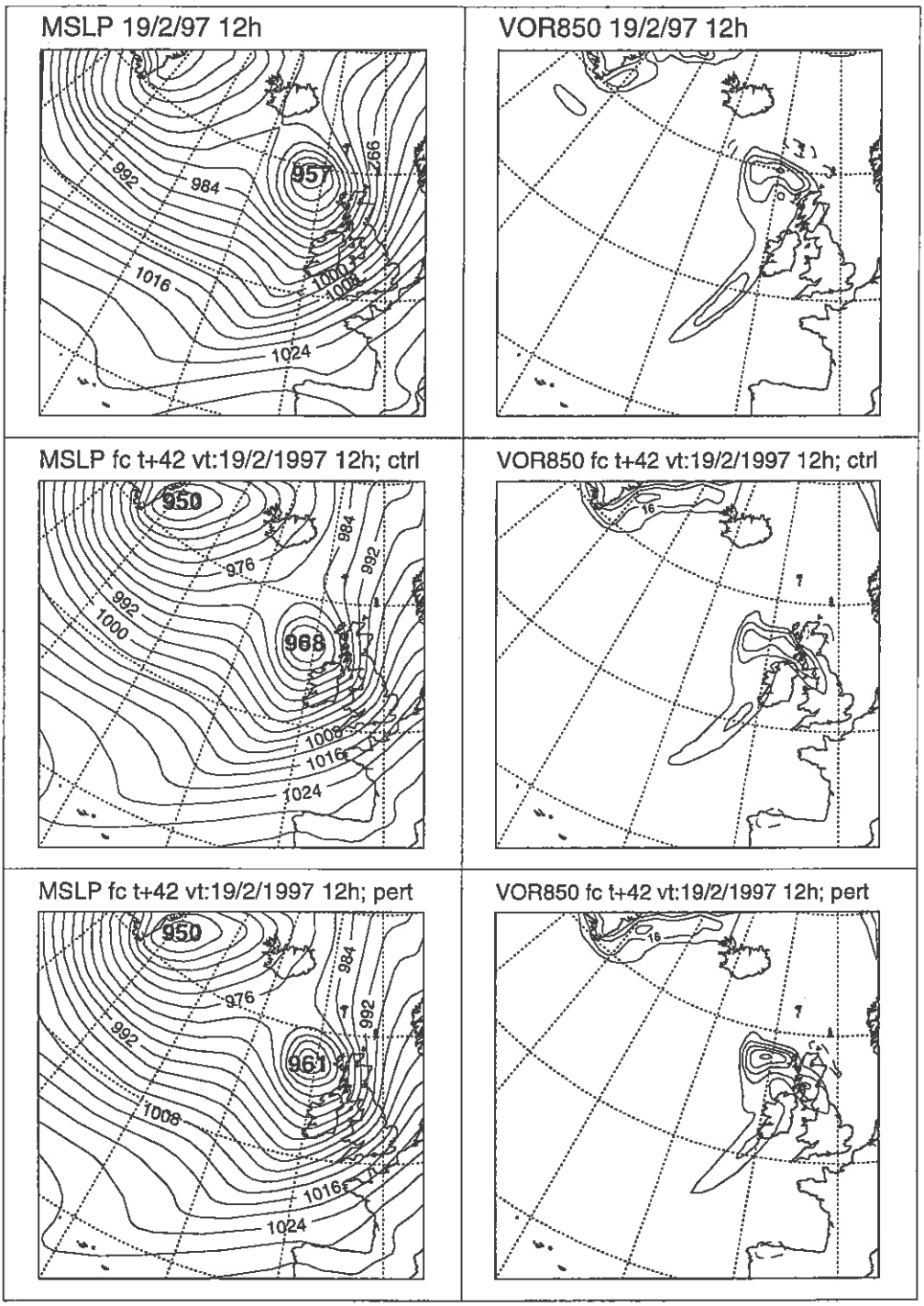
MSLP 19/2/97 12h
VOR850 19/2/97 12h
MSLP fc t+42 vt:19/2/1997 12h; ctrl
VOR850 fc t+42 vt:19/2/1997 12h; ctrl
MSLP fc t+42 vt:19/2/1997 12h; pert
VOR850 fc t+42 vt:19/2/1997 12h; pert
950
957
961
968
976
984
992
1000
1008
1016
1024

FIG. 5

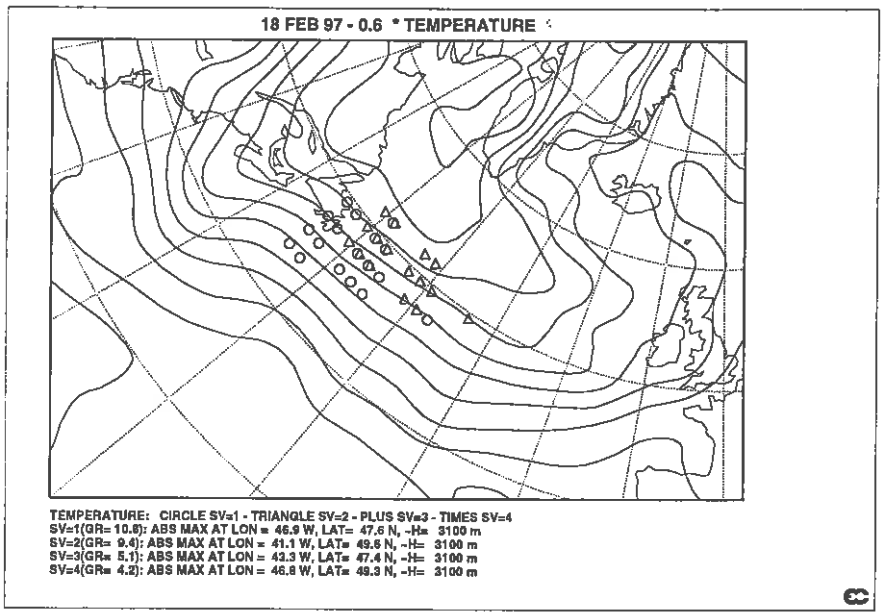
18 FEB 97 - 0.6 * TEMPERATURE
TEMPERATURE: CIRCLE SV=1 - TRIANGLE SV=2 - PLUS SV=3 - TIMES SV=4
SV=1(GR= 10.6): ABS MAX AT LON = 46.9 W, LAT= 47.6 N, -H= 3100 m
SV=2(GR= 9.4): ABS MAX AT LON = 41.1 W, LAT= 49.6 N, -H= 3100 m
SV=3(GR= 5.1): ABS MAX AT LON = 43.3 W, LAT= 47.4 N, -H= 3100 m
SV=4(GR= 4.2): ABS MAX AT LON = 46.8 W, LAT= 49.3 N, -H= 3100 m

FIG. 7

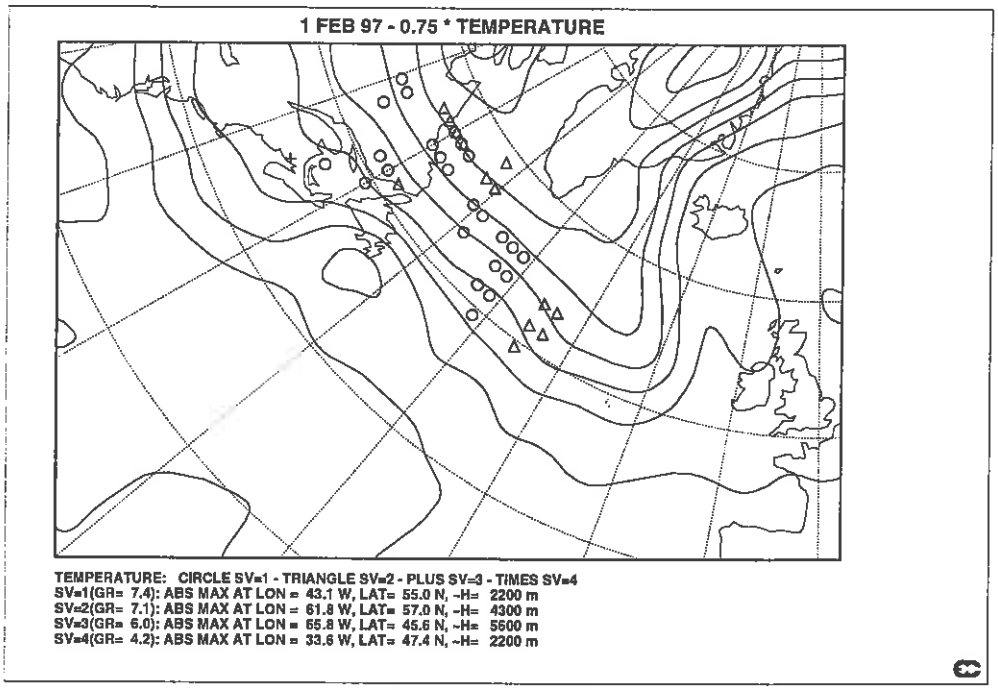
1 FEB 97 - 0.75 * TEMPERATURE
TEMPERATURE: CIRCLE SV=1 - TRIANGLE SV=2 - PLUS SV=3 - TIMES SV=4
SV=1(GR= 7.4): ABS MAX AT LON = 43.1 W, LAT= 55.0 N, ~H= 2200 m
SV=2(GR= 7.1): ABS MAX AT LON = 61.8 W, LAT= 57.0 N, ~H= 4300 m
SV=3(GR= 6.0): ABS MAX AT LON = 65.8 W, LAT= 45.6 N, ~H= 5600 m
SV=4(GR= 4.2): ABS MAX AT LON = 33.6 W, LAT= 47.4 N, ~H= 2200 m

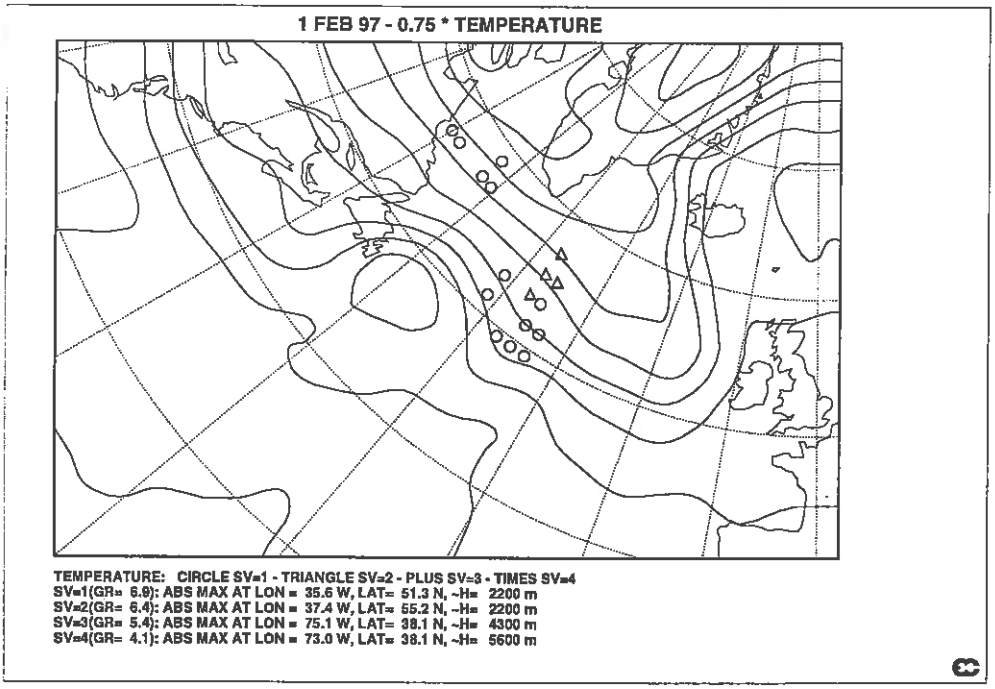
1 FEB 97 - 0.75 * TEMPERATURE
TEMPERATURE: CIRCLE SV=1 - TRIANGLE SV=2 - PLUS SV=3 - TIMES SV=4
SV=1(GR= 6.9): ABS MAX AT LON = 35.6 W, LAT= 51.3 N, ~H= 2200 m
SV=2(GR= 6.4): ABS MAX AT LON = 37.4 W, LAT= 55.2 N, ~H= 2200 m
SV=3(GR= 5.4): ABS MAX AT LON = 75.1 W, LAT= 38.1 N, ~H= 4300 m
SV=4(GR= 4.1): ABS MAX AT LON = 73.0 W, LAT= 38.1 N, ~H= 5600 m

FIG. 9

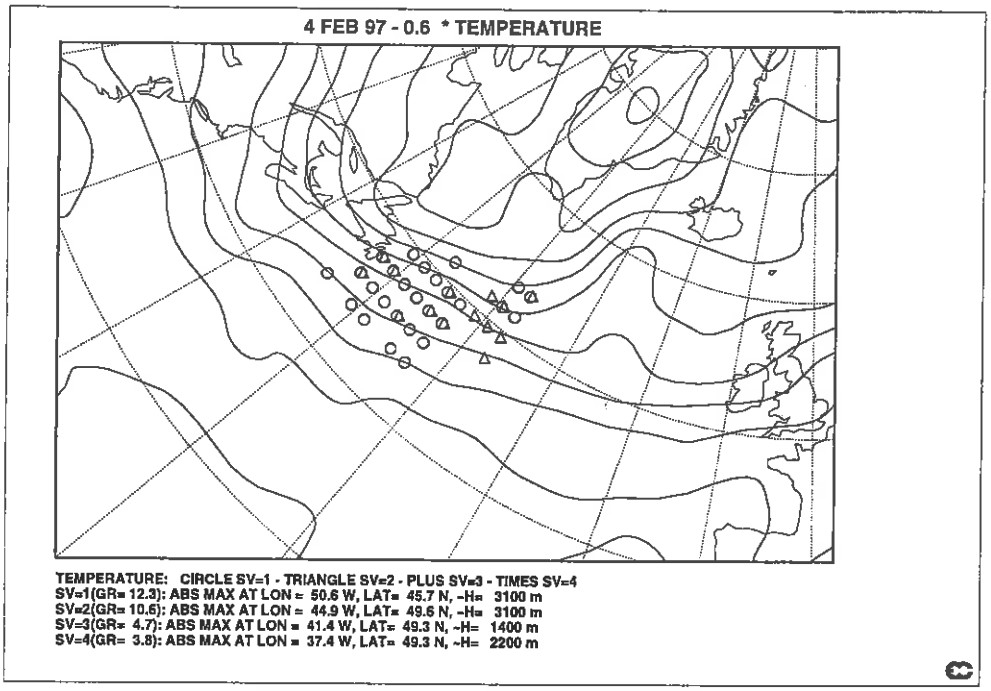
4 FEB 97 - 0.6 * TEMPERATURE
TEMPERATURE: CIRCLE SV=1 - TRIANGLE SV=2 - PLUS SV=3 - TIMES SV=4
SV=1(GR= 12.3): ABS MAX AT LON = 50.6 W, LAT= 45.7 N, -H= 3100 m
SV=2(GR= 10.6): ABS MAX AT LON = 44.9 W, LAT= 49.6 N, -H= 3100 m
SV=3(GR= 4.7): ABS MAX AT LON = 41.4 W, LAT= 49.3 N, -H= 1400 m
SV=4(GR= 3.8): ABS MAX AT LON = 37.4 W, LAT= 49.3 N, -H= 2200 m

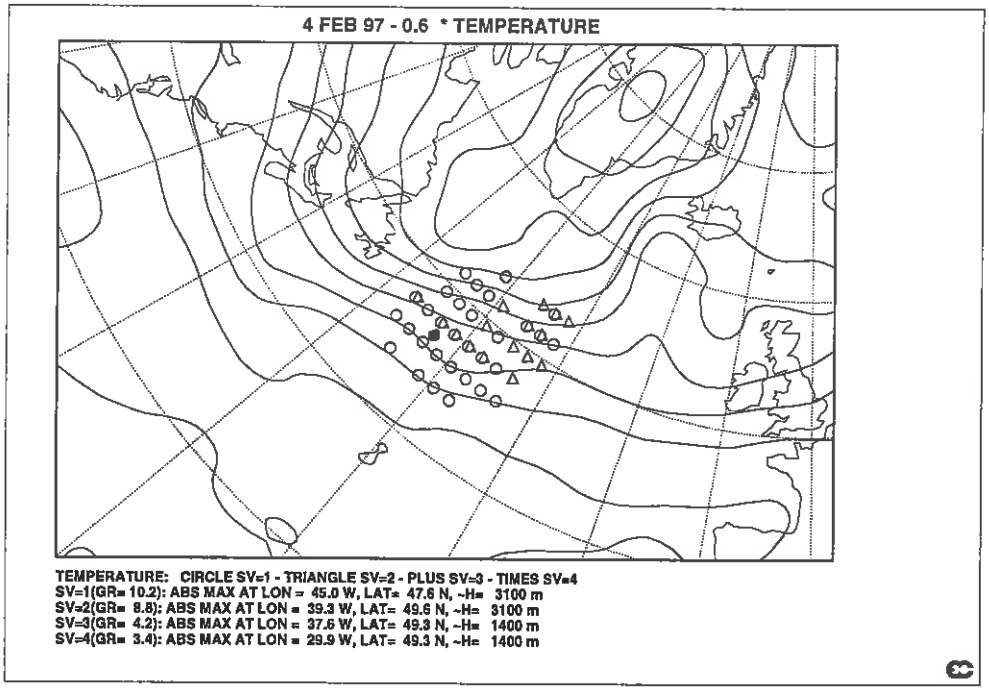
4 FEB 97 - 0.6 * TEMPERATURE
TEMPERATURE: CIRCLE SV=1 - TRIANGLE SV=2 - PLUS SV=3 - TIMES SV=4
SV=1(GR= 10.2): ABS MAX AT LON = 45.0 W, LAT= 47.6 N, -H= 3100 m
SV=2(GR= 8.8): ABS MAX AT LON = 39.3 W, LAT= 49.6 N, -H= 3100 m
SV=3(GR= 4.2): ABS MAX AT LON = 37.6 W, LAT= 49.3 N, -H= 1400 m
SV=4(GR= 3.4): ABS MAX AT LON = 29.9 W, LAT= 49.3 N, -H= 1400 m

FIG. 11

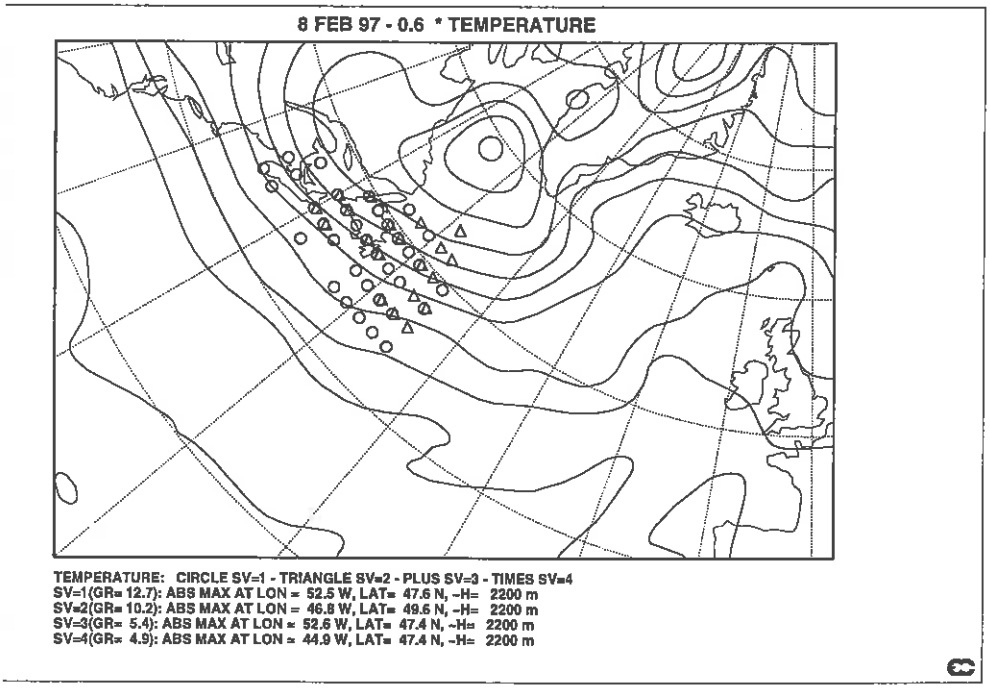
8 FEB 97 - 0.6 * TEMPERATURE
TEMPERATURE: CIRCLE SV=1 - TRIANGLE SV=2 - PLUS SV=3 - TIMES SV=4
SV=1(GR= 12.7): ABS MAX AT LON = 52.5 W, LAT= 47.6 N, -H= 2200 m
SV=2(GR= 10.2): ABS MAX AT LON = 46.8 W, LAT= 49.6 N, -H= 2200 m
SV=3(GR= 5.4): ABS MAX AT LON = 52.6 W, LAT= 47.4 N, -H= 2200 m
SV=4(GR= 4.9): ABS MAX AT LON = 44.9 W, LAT= 47.4 N, -H= 2200 m

FIG 13

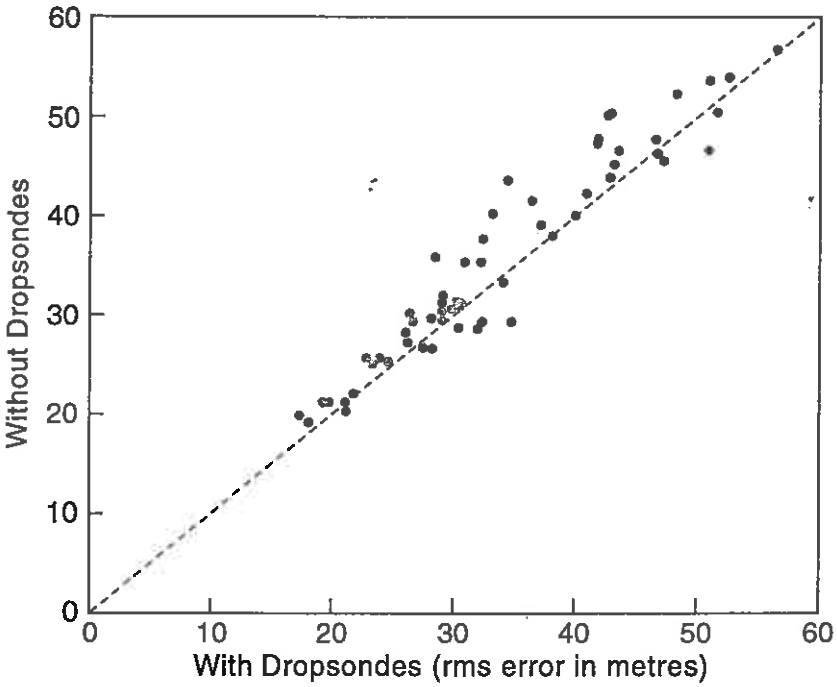
Without Dropsondes
With Dropsondes (rms error in metres)
0
10
20
30
40
50
60

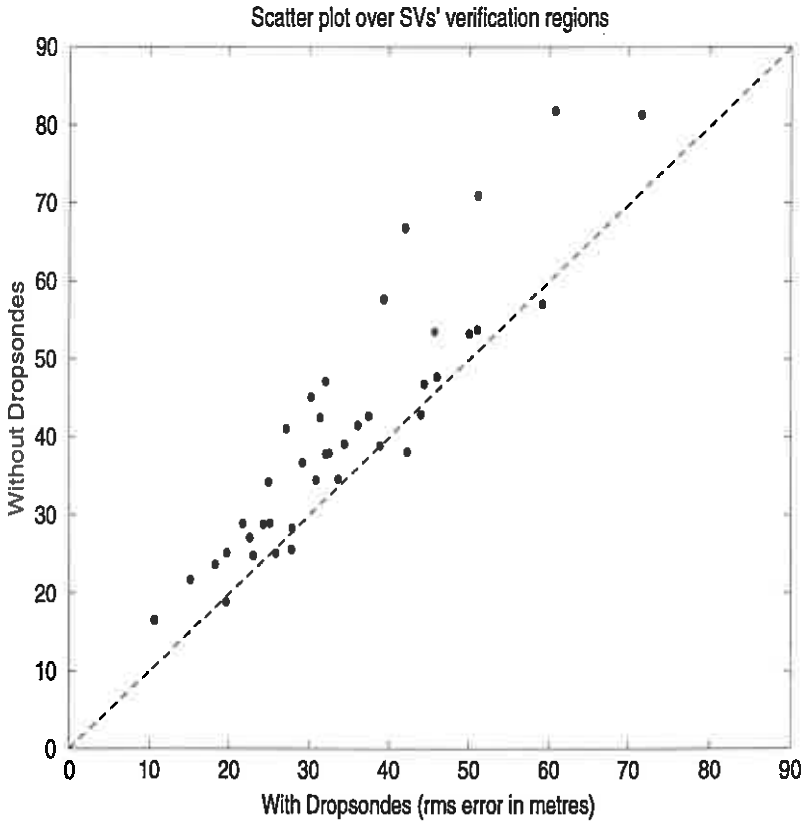
Scatter plot over SVs' verification regions
Without Dropsondes
With Dropsondes (rms error in metres)
0
10
20
30
40
50
60
70
80
90

FIG. 15

CURRENT JCMM INTERNAL REPORTS

This series of JCMM Internal Reports, initiated in 1993, contains unpublished reports and also versions of articles submitted for publication. The complete set of Internal Reports is available from the National Meteorological Library on loan, if required.

1. **Research strategy and programme**
   K A Browning et al
   January 1993

2. **The GEWEX Cloud System Study (GCSS)**
   GEWEX Cloud System Science Team
   January 1993

3. **Evolution of a mesoscale upper tropospheric vorticity maximum and comma cloud from a cloud-free two dimensional potential vorticity anomaly**
   K A Browning
   January 1993

4. **The global energy and water cycle**
   K A Browning
   July 1993

5. **Structure of a midlatitude cyclone before occlusion**
   K A Browning and N Roberts
   July 1993

6. **Developments in systems and tools for weather forecasting**
   K A Browning and G Szejwach
   July 1993

7. **Diagnostic study of a narrow cold frontal rainband and severe winds associated with a stratospheric intrusion**
   K A Browning and R Reynolds
   August 1993

8. **Survey of perceived priority issues in the parametrizations of cloud-related processes in GCMs**
   K A Browning
   September 1993

9. **The effect of rain on longwave radiation**
   I Dharssi
   September 1993

10. **Cloud microphysical processes - a description of the parametrization used in the large eddy model**
    H Swann
    October 1993

11. **An appreciation of the meteorological research of Ernst Kleinschmidt**
    A J Thorpe
    May 1992

12. **Potential vorticity of flow along the Alps**
    A J Thorpe, H Volkert and Dietrich Heimann
    August 1992

13. **The representation of fronts**
    A J Thorpe
    January 1993

29. **Mesoscale effects of a dry intrusion within a vigorous cyclone**
K A Browning and B W Golding
April 1994

30. **GEWEX Cloud System Study, Science Plan**
May 1994

31. **Parametrization of momentum transport by convectively generated gravity waves**
R Kershaw
May 1994

32. **Mesoscale Modelling Newsletter No 5**
May 1994

33. **Observations of the mesoscale sub-structure in the cold air of a developing frontal cyclone**
K A Browning, S A Clough, C S A Davitt, N M Roberts and T D Hewson
May 1994

34. **Longwave radiative forcing of a simulated tropical squall line**
Imtiaz Dharssi
July 1994

35. **On the nature of the convective circulation at a kata-cold front**
K A Browning
September 1994

36. **Collective preprints of papers submitted to the COST-75 International Seminar on Advanced Weather Radar Systems, Brussels, 20-23 September 1994**
November 1994

37. **Use of satellite imagery to diagnose events leading to frontal thunderstorms: Parts I and II of a case study**
K A Browning and N M Roberts
November 1994

38. **The role of spaceborne millimetre-wave radar in the global monitoring of ice cloud**
P R A Brown, A J Illingworth, A J Heymsfield, G M McFarquhar, K A Browning and M Gosset
December 1994

39. **Potential vorticity inversion**
Michal Ziemianski
October 1994

40. **Theory of mature tropical cyclones; a comparison between Kleinschmidt (1951) and Emanuel (1986)**
Suzanne L Gray
December 1994

41. **Dispersion and removal of pollutants during the passage of an atmospheric frontal system**
N R Gimson
December 1994

42. **The role of snow sublimation in frontogenesis**
D J Parker and A J Thorpe
December 1994

43. **Potential vorticity and the electrostatics Analogy: Ertel-Rossby formulation**
A J Thorpe and C H Bishop
December 1994

59. **Investigation of different representations of rain in a 1-d evaporation model**
H Swann
May 1996

60. **Parametrization of diabatic processes in the inversion of the omega-equation**
M Athanassiadou and A J Thorpe
June 1996

61. **The role of the environmental flow in the development of secondary frontal cyclones**
I A Renfrew, A J Thorpe and A Joly
June 1996

62. **Consequences of the geostrophic momentum approximation on barotropic instability**
S Malardel, A J Thorpe and A Joly
June 1996

63. **Contributions to the AMS/RMS Conference on Mesoscale Processes**
Reading, 9-13 September 1996

64. **Vorticity and potential vorticity in stratified flows interacting with an isolated obstacle**
Jorge A Gutiérrez and A J Thorpe
September 1996

65. **Triple point development: two case studies**
Douglas Parker
September 1996

66. **Radar observations of wind-shear splitting within evolving atmospheric Kelvin-Helmholtz billows**
D Chapman and K A Browning
April 1997

67. **Cold frontal structure derived from radar wind profilers**
K A Browning, D Jerrett, J Nash, T Oakley and N M Roberts
May 1997

68. **The dry intrusion and its effect on the frontal, cloud and precipitation structure of extratropical cyclones**
K A Browning - Text of invited special lecture at the Spring Conference
of the Meteorological Society of Japan, University of Tsukuba, 22 May 1997

69. **Met. Office Unified Model data, diagnostics, graphics programs, and other observational data available from the JCMM through the aegis of the Universities Weather Research Network (UWERN).** (Plus supplement)
Peter Panagi and Ed Dicks
June 1997

70. **Contributions of the JCMM/Dept of Meteorology Radar Group to the 28th AMS Radar Meteorology Conference.** Austin, Texas
September 1997

71. **Sensitivity of short-range weather forecasts to local potential vorticity modifications**
Meral Demirtas and Alan Thorpe
July 1997

72. **Objective identification of frontal wave cyclones**
T D Hewson
August 1997

73. **Attribution and its application to mesoscale structure associated with tropopause folds**
A J Thorpe
September 1997

88. **Radar estimates of rainfall rates at the ground in bright band and non-bright band events**
T J Smyth and A J Illingworth
June 1998

89. **Correction for attenuation of radar reflectivity using polarisation data**
T J Smyth and A J Illingworth
June 1998

90. **The effects of convection on chemical reactions and precipitation scavenging**
Neil R Gimson
July 1998

91. **How to use the display program DISP**
Nigel Roberts
August 1998

92. **Conceptual models of cyclogenesis**
Adrian T Semple
August 1998

93. **Observations of oblate hail using dual polarisation radar and implications for hail detection schemes**
T J Smyth, T M Blackman and A J Illingworth
September 1998

94. **The semigeostrophic diagnosis of vertical motion. Part I: Formulation and co-ordinate transformations**
Mike A Pedder and Alan J Thorpe
September 1998

95. **The semigeostrophic diagnosis of vertical motion. Part II: Results for an idealised baroclinic wave life cycle**
Alan J Thorpe and Mike A Pedder
September 1998

96. **Convective destabilisation by a tropopause fold diagnosed using potential vorticity inversion**
Morwenna Griffiths, Alan Thorpe and Keith Browning
October 1998

97. **Forecast skill of the ECMWF model using targeted observations during FASTEX**
A Montani, A J Thorpe, R Buizza and P Unden
October 1998

Met Office Joint Centre for Mesoscale Meteorology Department of Meteorology
University of Reading PO Box 243 Reading RG6 6BB United Kingdom
Tel: +44 (0)118 931 8425 Fax: +44 (0)118 931 8791
www.metoffice.com